



# One-pot synthesis of multifunctional ZnO nanomaterials: study of superhydrophobicity and UV photosensing property

R. Ghosh<sup>1</sup> · S. Kundu<sup>1</sup> · R. Majumder<sup>1</sup> · S. Roy<sup>4</sup> · S. Das<sup>3</sup> · A. Banerjee<sup>3</sup> · U. Guria<sup>2</sup> · M. Banerjee<sup>2</sup> · M. K. Bera<sup>2</sup> · Kiran M. Subhedar<sup>5</sup> · M. Pal Chowdhury<sup>1</sup>

Received: 12 January 2019 / Accepted: 14 February 2019 / Published online: 4 March 2019  
© King Abdulaziz City for Science and Technology 2019

## Abstract

ZnO nanomaterials are synthesized using one-pot synthesis method. Equimolar solution of Zinc Nitrate hexahydrate ( $\text{Zn}(\text{NO}_3)_2 \cdot 6\text{H}_2\text{O}$ ) and Hexamethylenetetramine ( $\text{C}_6\text{H}_{12}\text{N}_4$ ) is used as a precursor for ZnO formation. Different nanostructures of ZnO are achieved by controlling the pH of the growth solution in the range 2–12 (acidic to alkali). ZnO nanostructures are evaluated for hydrophobic property using static contact angle measurement setup and UV photosensing activity. Surface morphology, structural properties and compositional analysis of ZnO nanostructures are examined by field emission scanning electron microscope (FE-SEM), energy dispersive X-ray analysis (EDX), high-resolution transmission electron microscope (FEG-TEM) and X-ray diffraction (XRD) measurements. Existence of ZnO wurtzite structure is confirmed from XRD study and is analyzed by Rietveld refinement method. Nanomaterials are characterized using Raman spectroscopy which confirms highest oxygen deficiency in ZnO nanorods. The material shows remarkable superhydrophobic and UV photosensing property and hence the name multifunctional. Among all morphologies grown at different pH values, ZnO nanorods show superhydrophobic nature with contact angle more than  $170^\circ$ . Total surface energy value of ZnO nanostructures is calculated using Wendt two-component theory. Different ZnO nanostructures (with variation of pH value) are used to study UV photosensing property. Responsivity and photocurrent show a strong dependence on the morphology of ZnO.

**Keywords** ZnO · pH · Superhydrophobic · Surface energy · Photocurrent · Responsivity

## Introduction

In recent years, one-dimensional (1D) nanoscale materials (Djurišić et al. 2012; Khranovsky and Yakimova 2012; Zhang et al. 2012a, b, c, 2013, 2016a, b, c, 2017a, b; Wang et al. 2018) have received considerable attention due to their remarkable properties (Kundu et al. 2019) that are useful

in antimicrobial activity (Chen et al. 2019; Dimapilis et al. 2018; Smeraldi et al. 2017), optoelectronic (Chang et al. 2012; Wang 2004; Orlov et al. 2016) and nanoelectronic devices (Prakash et al. 2008; Park et al. 2016; Peng et al. 2018), and electrochemical and electromechanical devices (Sarangi 2016; Sarahnaz et al. 2013; Sun and Sirringhaus 2005; Choi et al. 2009; Zhang et al. 2016a, b, c, 2015). ZnO nanomaterials such as ZnO nanorods (Sun et al. 2006), ZnO nanoneedles (Zhang et al. 2013a, b), ZnO nanoflowers (Wahab et al. 2007; Khokra et al. 2017; Kumar et al. 2019) have been intensively investigated in environmental applications (Zanni et al. 2017; Zhang et al. 2019, 2018; Medina et al. 2018; Sirelkhatim et al. 2015; Udom et al. 2013) due to their remarkable properties, e.g., wide direct-band gap ( $E_g$  3.37 eV), large exciton binding energy (60 meV) and high melting point. ZnO nanomaterial is a potential candidate for application in UV sensing device due to size effect, surface chemistry and its band gap value which is in the intermediate region between UV and visible light (Sarkar and Basak 2015). Researchers have used a variety

✉ M. Pal Chowdhury  
manishpc@gmail.com

<sup>1</sup> Department of Physics, IEST, Shibpur, Howrah 711103, India  
<sup>2</sup> Department of Chemistry, IEST, Shibpur, Howrah 711103, India  
<sup>3</sup> Department of Physics, University of Calcutta, Kolkata 700009, India  
<sup>4</sup> Department of Physics, Jadavpur University, Kolkata 700032, India  
<sup>5</sup> Advanced Carbon Products group, CSIR-National Physical Laboratory, New Delhi 110012, India

of synthesis techniques, e.g., chemical vapor deposition, template-mediated growth, hydrothermal, and evaporation for ZnO nanostructure synthesis. These techniques use either high operating temperature or high pressure or prolonged growth time or sophisticated instruments. Superhydrophobic surfaces have grabbed tremendous attention due to its potential applications (Li et al. 2011; Wenzel 1936; Sasmal et al. 2014; Lee et al. 2011). ZnO nanostructures grown on sodalime glass substrate with contact angle more than  $170^\circ$  show a good hydrophobic property (Vicente et al. 2012). The phenomenon of hydrophobicity can be well understood using Wendt two-component theory (Schuster et al. 2015). Due to high surface to volume ratio, ZnO nanorods show better sensing property (Rodwihok et al. 2017; Shaikh et al. 2016; Soci et al. 2007) under UV-illuminated condition.

The aim of this work is to demonstrate the preparation of ZnO nanostructures by one-pot synthesis method and to study its multifunctional activity. Static contact angle measurement and calculation of surface free energy are performed for all ZnO nanostructures to know the hydrophobic nature of the nanomaterials. Photosensing properties of ZnO nanostructures are studied with variation of pH value. From the measured data photocurrent, responsivity and time constants of photocurrent growth and decay processes are calculated.

## Experimental details

### Synthesis of ZnO nanostructure

#### Preparation of ZnO seed layer solution

ZnO nanostructures are synthesized using one-pot synthesis method. For seed layer deposition, the ZnO seed layer solution is prepared using zinc nitrate hexahydrate ( $\text{Zn}(\text{NO}_3)_2 \cdot 6\text{H}_2\text{O}$ ) and hexamethylenetetramine ( $\text{C}_6\text{H}_{12}\text{N}_4$ ) as precursors and ethanol ( $\text{C}_2\text{H}_5\text{OH}$ ) as solvent. All the chemicals are of analytical grade and purchased from Fisher scientific and used without further purification. ZnO solution is obtained by mixing equimolar quantity of zinc nitrate hexahydrate and hexamethylenetetramine with 20 ml of solvent.

#### Deposition of ZnO seed layer

In this experiment, sodalime glass is used as the substrate. Before ZnO seed layer deposition process, standard substrate cleaning procedure is followed, where the substrate is cleaned in soap solution, rinsed in deionised water and finally sonicated in isopropyl alcohol ( $\text{C}_3\text{H}_8\text{O}$ ) for 60 s and dried in nitrogen flow. After that spin coater is used to deposit the ZnO seed layer solution on the precleaned glass substrates at 2000 rpm for 60 s followed by annealing process in a hot oven at  $350^\circ\text{C}$  for 10 min.

### ZnO nanostructures formation

After deposition of the seed layer coating on glass substrate, the ZnO nanostructures are obtained through solution-based growth method. The equimolar growth solution of zinc nitrate hexahydrate ( $\text{Zn}(\text{NO}_3)_2 \cdot 6\text{H}_2\text{O}$ ) and hexamethylenetetramine ( $\text{C}_6\text{H}_{12}\text{N}_4$ ) is prepared in deionized water. The ZnO nanostructures are grown by immersing the substrate in the aqueous solution. pH of the solution in the range 2–12 (alkali–acidic) is achieved by gradually adding ammonium hydroxide ( $\text{NH}_4\text{OH}$ ) and hydrochloric acid (HCl) respectively. pH value of the solution is measured using pH meter. During the growth process, the aqueous solution is heated at  $90^\circ\text{C}$  for 4 h on a hot plate. After the growth process, the sample is removed from solution and rinsed in deionised water followed by drying in air at room temperature.

The morphological change of the material is characterized by FE-SEM (INSPECT F50, Netherland) and FEG-TEM (JEM-2100F). Structural analysis is performed using X-Ray diffractometer (Model No.: X'Pert Powder, PANalytical) with  $\text{CuK}_\alpha$  radiation of wavelength 0.015418 nm. Chemical compositional analysis is done using energy dispersive X-ray analysis (EDX). Chemical environment analysis is done using FTIR (Jasco FT/IR-4600). Band-gap energy calculation is done using UV–VIS (UV-1800 SHIMADZU UV SPECTROPHOTOMETER). ZnO nanostructures are also characterized using Raman spectroscopy (Renishaw—InVia Raman Microscope equipped with a 514 nm wavelength excitation laser and 2400 lines/mm grating. A laser beam size of  $\sim 1\ \mu\text{m}$  with  $\times 50$  objective lens is used.)

### Static contact angle measurement

Schematic of the static contact angle measurement setup is shown in Fig. 1. The diffuse light from a white LED light source passing through the liquid droplet resting on the substrate surface is captured by CMOS camera (Micaps) using image acquisition software. The images captured are analyzed by LBADSA method based on the fitting of the Young–Laplace equation using Java plug-in (Shahabi et al. 2014) from the ImageJ software for static contact angle measurement. The substrate is placed under the liquid drop dispenser on a 3-axis ( $xyz$ ) micropositioner. The alignment of the travelling microscope and the sample stage is achieved using the micropositioner. The volume of the droplet formed is  $6\ \mu\text{l}$ . The droplet is formed by pushing probe liquid by a syringe manually. Surface free energy of the substrate is estimated using three probe liquids, water, glycerol and ethylene glycol. The static contact angle of the liquid drops (water, ethylene glycol and glycerol) is measured using the low-bond axisymmetric drop shape analysis tool of ImageJ software (Stalder et al. 2010).

**Fig. 1** Schematic diagram of static contact angle measurement setup

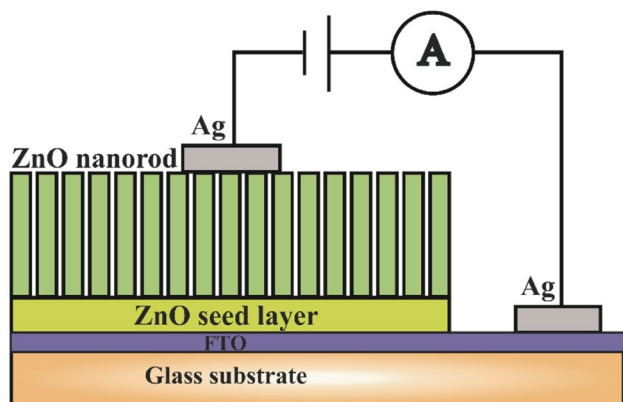
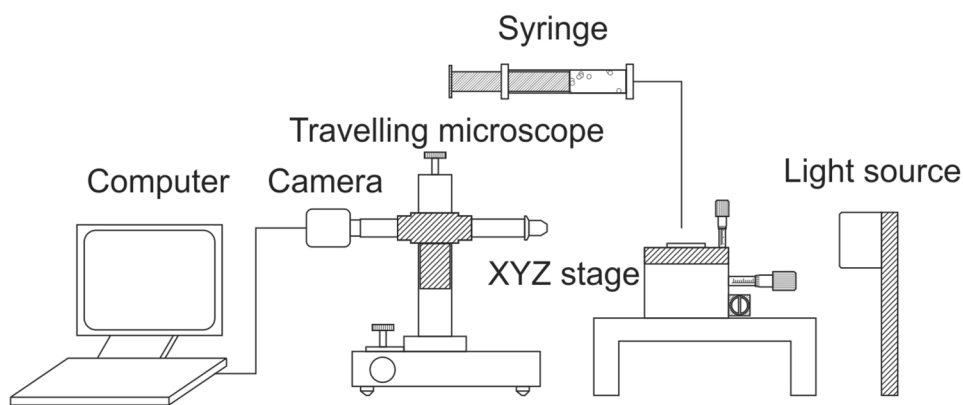


**Fig. 2** Schematic diagram of fabricated UV photosensor using ZnO nanostructure

**Device fabrication for UV photosensor**

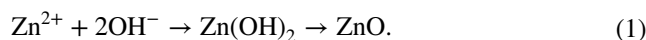
Schematic diagram of the fabricated UV sensor having FTO/ZnO/Ag structure is shown in Fig. 2. ZnO nanostructures (with variation of pH value) are grown on FTO glass substrate as described in experimental details. Electrodes are drawn on FTO and ZnO surface using silver (Ag) paste.

**Results**

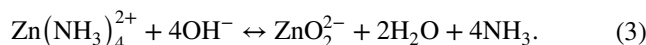
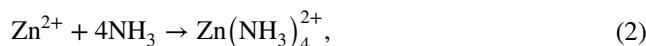
**Morphology and chemical composition**

FESEM images of ZnO nanostructures grown at four different pH values are shown in Fig. 3a–d. At pH 6, typical highly oriented vertical hexagonal nanorods are grown. As there is no space to grow laterally, the nanorods grow vertically forming nanorod forest. With higher HCl concentration (pH 1), ZnO nanomaterials are completely etched out. Under the described growth condition, maximum value of pH 12 is achieved by adding NH<sub>4</sub>Cl. With increase in pH value, microstructure displays transition from hexagonal

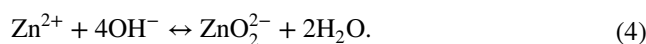
nanorods (pH 6) to modified nanorods (pH 9) and then to pointed nanorods (pH 11.5). pH values are gradually increased by adding ammonium hydroxide solution into the stock solution. With the addition of ammonium hydroxide, insoluble Zn(OH)<sub>2</sub> is produced, which is indicated by the whitish solution. pH of the growth solution is maintained in the range 6–7 to synthesize nanorods, which can be explained with the following reaction mechanism (Demianets et al. 2002; Yin et al. 2011):



Further, addition of ammonium hydroxide solution, Zn(OH)<sub>2</sub> dissolves to form a soluble complex of zinc hydroxide [Zn(OH)<sub>4</sub>]<sup>2+</sup>, which leads to the formation of zincate ions Zn[(OH)<sub>4</sub>]<sup>2-</sup>:



Therefore, the overall reaction leading to the formation of zincate ions is



Further, zincate ions react with hot water to give ZnO.



Catalyst particles, deposited on the substrate oriented along <0001> direction with positively charged polar Zn<sup>+</sup> plane, adsorb zincate complex and predominant growth of the c-axis occurs. The growth rate of different ZnO planes occurs according to (0001)> (0110)> (0001̄) (Sohn et al. 2014). (<102>), (<110>), (<103>) and (<200>) planes as shown in Fig. 7 have slow growth rate and hexagonal nanorods are formed. Further increase in the pH value (pH 9) results in flower-like structure growth on the substrate. At higher pH value, seed particles in the solution coagulate to have reduced surface energy (Li et al. 1999; Yin et al. 2014).

**Fig. 3** SEM images of ZnO nanostructure grown for different pH value: **a** 3, **b** 6, **c** 9, **d** 11.5

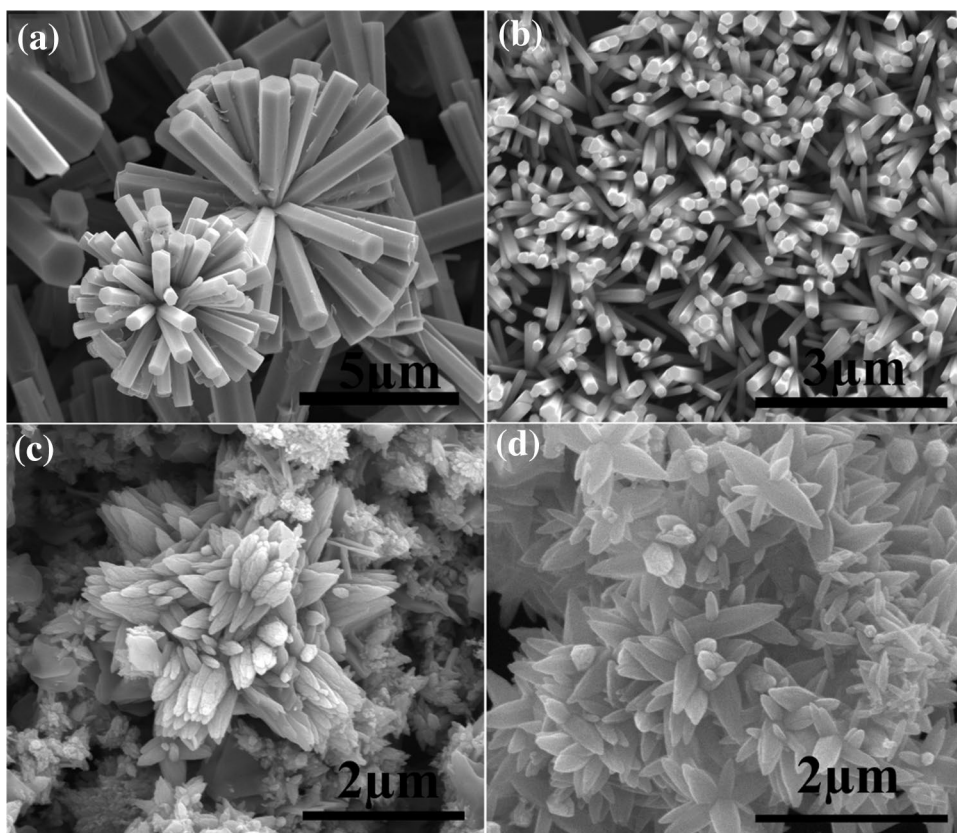
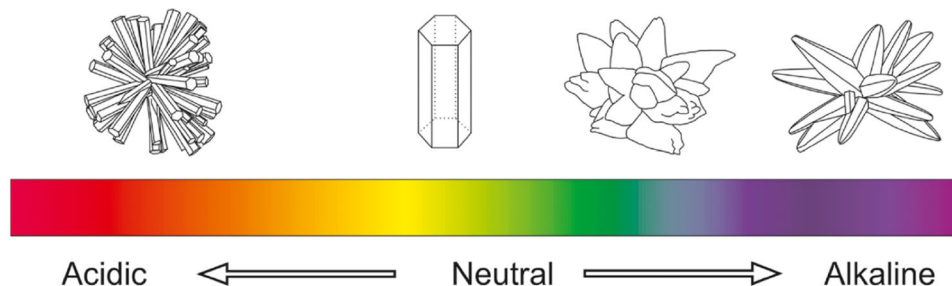


**Fig. 4** Schematic diagram for structural variation of ZnO with variation of pH values



At higher pH values (pH 8.5, 9.5, 10.5 and 11.5), ZnO seed particles show aggregation (Mudunkotuwa et al. 2012) and from the active growth centers ZnO starts to grow in accordance with the seed crystallites. At pH 9, colour of the bath solution turned whitish as a result of insoluble  $\text{Zn}(\text{OH})_2$ . With the addition of ammonium hydroxide solution, soluble complex zinc hydroxide ion and tetraamine zincate are produced which react with water to give  $\text{Zn}(\text{OH})_2$ . With the increase of alkaline nature, concentration of  $\text{OH}^-$  ions increases in the solution which is responsible for the growth of ZnO. At pH 9, the flower formation is at its beginning stage, the petal-like structures are not fully formed (Fig. 3c). Figure 3d shows growth at pH value 11.5 and shape of the petal-like structure of flowers becomes uniform due to high concentration of  $\text{OH}^-$  and hence Ostwald

ripening. pH values of the acidic region of the growth solution are achieved by adding hydrochloric acid in the bath. Typical microstructure of ZnO films at pH 6 is represented in Fig. 3b, respectively. Under this growth condition, nanorods split into multiple rods to minimize surface free energy of the polar faces (0001), thereby forming bur-flower like structure. Morphologies of ZnO nanostructure are obtained under various growth conditions is illustrated in Fig. 4 with variation of pH value. The structure is changed from bur-flower to rod and finally from rod to modified flower.

EDX characterization (Fig. 5) of ZnO nanorods (pH 6) represents chemical composition of the sample. Figure 7a reveals that the nanorods are composed of Zn and O. No evidence of other impurities is found in the data. Elemental mapping of typical ZnO nanorods (pH 6) gives the overall

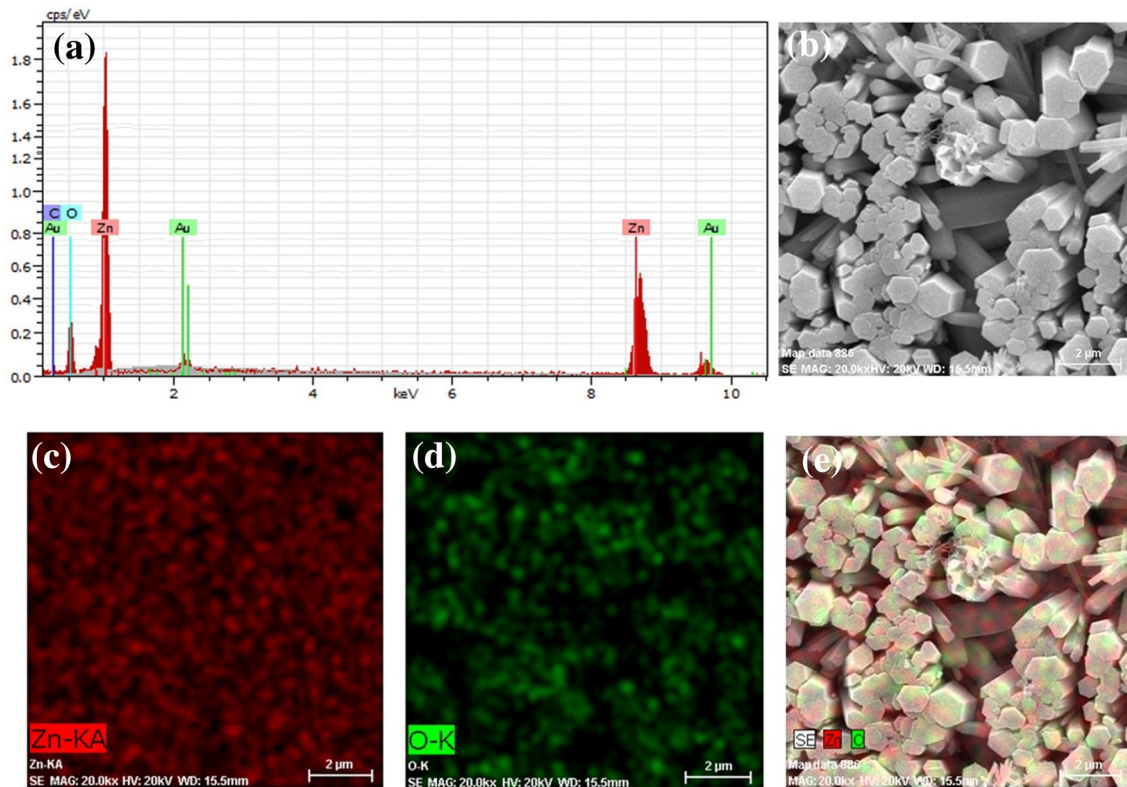


**Fig. 5** **a** EDX graph shows the presence of components in the sample (pH 6). **b** SEM image of typical ZnO nanorods. EDX mapping of **c** Zn, **d** O and **e** O and Zn combined for the sample region under investigation

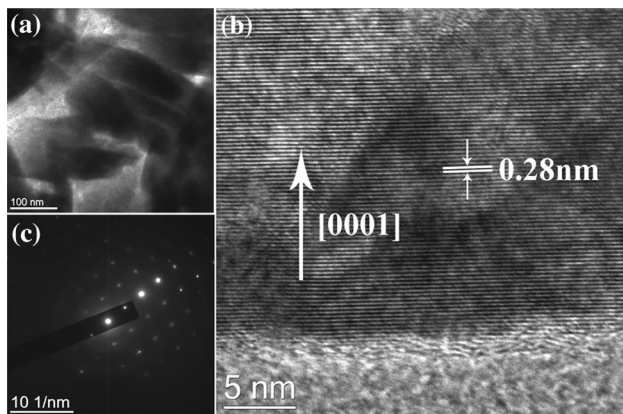


**Fig. 6** FEG-TEM image of **a** ZnO nanorods grown at pH 6. **b** ZnO nanorod lattice fringes with its **c** SAED (selected area electron diffraction) pattern

distribution of all the elements present in the sample as shown in Fig. 6c–e. As evidenced from the EDX mapping, Fig. 6c–e shows oxygen deficiency on the surface of ZnO nanorods.

Morphology and crystallinity of the ZnO sample grown at pH 6 are investigated using FEG-TEM. Figure 6a shows the TEM image of ZnO nanorods grown on soda lime glass

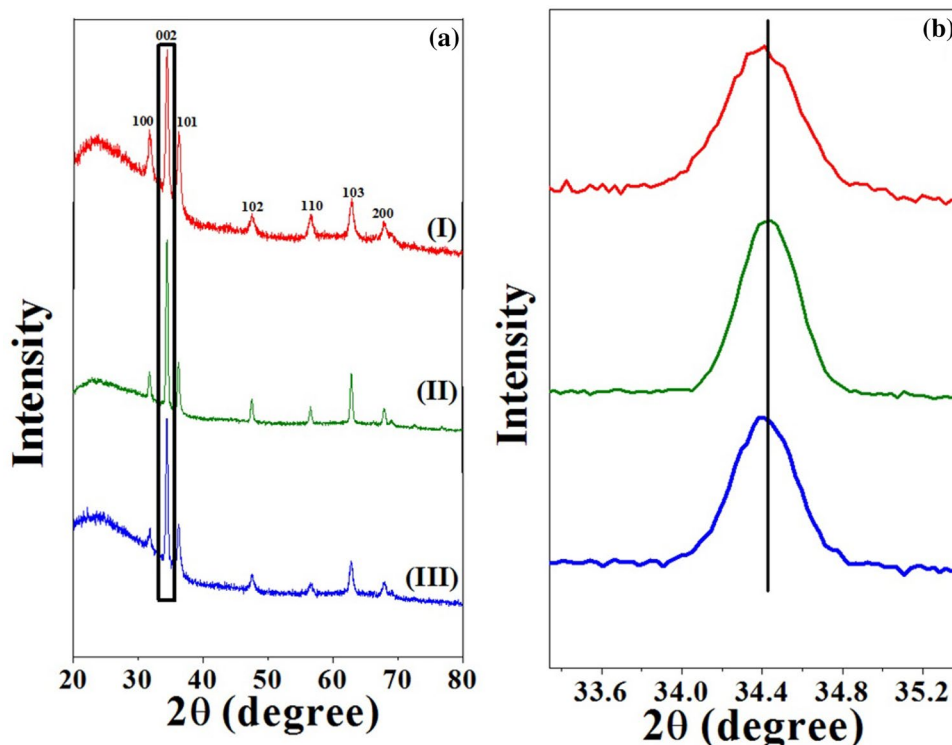
substrate. Typical diameters as measured from Fig. 6a are in the range 40–80 nm. The d-spacing value of 0.28 nm (Zhai et al. 2012) as estimated from the lattice fringes (Fig. 6b) corresponds to hexagonal wurtzite ZnO (100) planes (Agnihotri et al. 2015). The SAED (selected-area electron diffraction) pattern shown in Fig. 6c is in confirmation with the (100) lattice plane of ZnO hexagonal phase.

**XRD analysis**

Structural characterization of the ZnO nanostructures is performed by XRD, indicating a wurtzite structure (hexagonal phase, space group P63mc). All XRD measurements are performed at room temperature on thin film samples in the range  $20^\circ \leq 2\theta \leq 80^\circ$ . The XRD pattern of ZnO nanostructures (pH value 3, 6 and 10.5) as shown in Fig. 7I–III confirms the growth of wurtzite ZnO nanostructures. From Fig. 7a, it is well understood that the maximum growth occurs in <002> direction irrespective of pH value of the growth solution. It can be clearly seen from Fig. 7a that the sample is composed of single-phase wurtzite structure.

ZnO nanorods grown at pH 6 show selective *c* axis (<002>) growth in comparison with the materials grown under acidic and alkali pH condition. Other diffraction peaks, i.e., (100), (101), (102), (110), (103) and

**Fig. 7** **a** XRD pattern of grown ZnO nanostructures for pH value (I) 3, (II) 6 and (III) 10.5 respectively. **b** Shift of ( $\langle 002 \rangle$ ) for pH value 3, 6 and 10.5



(200), have been also detected and the intensity of the peaks implies the high crystallinity of the ZnO nanostructures. Shift of ( $\langle 002 \rangle$ ) for pH values 3, 6 and 10.5 has been shown in Fig. 7b.  $2\theta$  values for ( $\langle 002 \rangle$ ) are  $34.41^\circ$ ,  $34.44^\circ$  and  $34.38^\circ$ , respectively. For ZnO powder sample,  $2\theta$  value for ( $\langle 002 \rangle$ ) is  $34.5^\circ$  (Talam et al. 2012). The sample grown at pH 6 shows minimum shift followed by alkali (pH 10.5) and acidic (pH 3) region, respectively. Using Williamson–Hall (W–H) formula [ $\beta \cos \theta = (k\lambda/D) + 4\epsilon \sin \theta$ ] (where  $D$  is the domain size in nanometer,  $k$  is the shape factor (0.94),  $\lambda$  is the wavelength of  $\text{CuK}_\alpha$  radiation,  $\beta$  is the peak width at half maximum intensity,  $\epsilon$  is the weighted average strain) (Motevalizadeh et al. 2014), the domain size and micro-strain value are calculated for pH values 3, 6 and 10.5. Shift in  $2\theta$  value for ( $\langle 002 \rangle$ ) ensures the presence of compressive stress in the sample. MAUD software (Purwaningsih et al. 2016) is used for the refinement of XRD data for pH value 3, 6 and

10.5, respectively. Rietveld refinement dataset and dataset collected from W–H plot are summarized in Table 1.

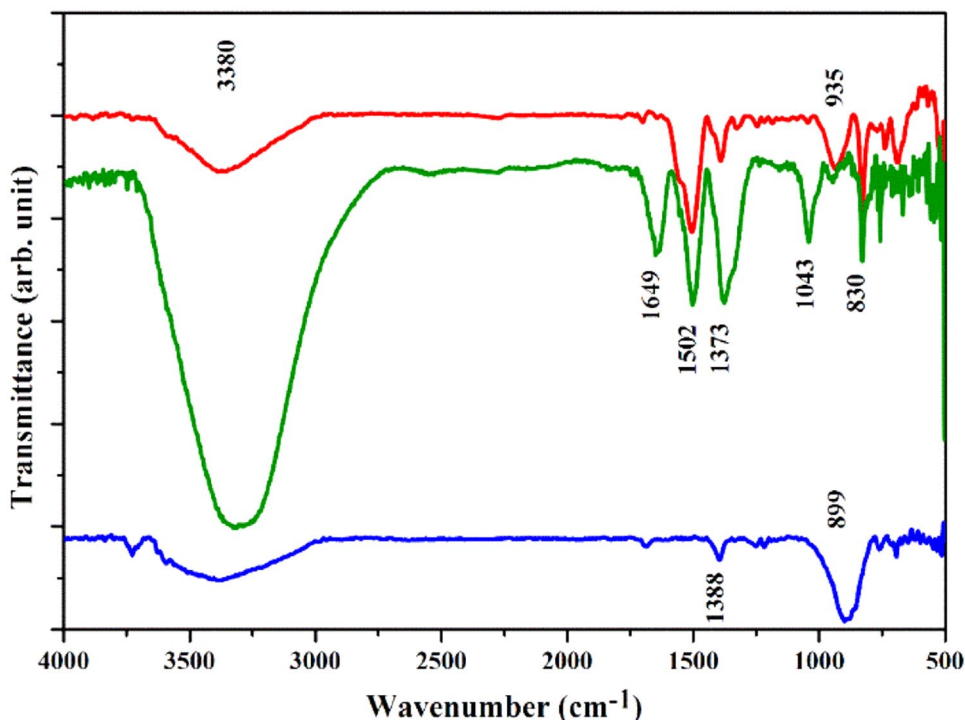
#### FTIR spectroscopy

FTIR measurement (Fig. 8) is performed at room temperature in the range  $500\text{--}4000\text{ cm}^{-1}$  for pH value 3, 6 and 10.5. The range ( $3100\text{--}3500\text{ cm}^{-1}$ ) corresponds to O–H mode stretching vibration of water (Tak et al. 2015; Chithra et al. 2015). Peak at  $1649\text{ cm}^{-1}$  represents vibration of carboxyl group (Ramimogshadam et al. 2013; Selvarajan and Mohanasrinivasan 2013). Peak at  $1375\text{ cm}^{-1}$  and  $1502\text{ cm}^{-1}$  ensures the presence of C–O bending mode. Deformation modes of  $\text{CH}_3$  group are visible at  $1043\text{ cm}^{-1}$  and O=C=O stretching modes are observed in the range  $800\text{--}900\text{ cm}^{-1}$ . N–H bending of primary amine is observed at  $1649\text{ cm}^{-1}$  which confirms the presence of  $\text{--NH}_2$  group (Doan et al. 2016).

**Table 1** Rietveld refinement dataset and W–H plot dataset for different pH values

pH value of ZnO samples	From Rietveld refinement						From W–H plot	
	Domain size (nm)	Strain* $10^{-4}$	$a$ (Å)	$c$ (Å)	$c/a$ ratio	Density ( $\text{g cm}^{-3}$ )	Domain size (nm)	Strain* $10^{-4}$
3	19	0.00267	3.2558	5.2151	1.601	5.6458	21	0.00232
6	26	0.00043	3.2556	5.2135	1.601	5.6481	27	0.00051
10.5	33	0.00239	3.2556	5.2135	1.601	5.6481	41	0.00300

**Fig. 8** FTIR spectra of ZnO nanostructure for pH value 3 (red line), 6 (green line), 10.5 (blue line)



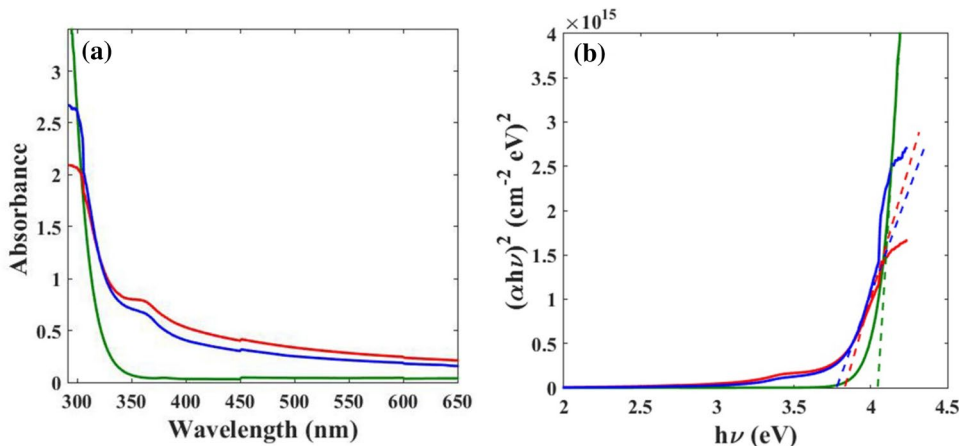
**UV-VIS**

Absorption spectra of the ZnO nanomaterials are shown in Fig. 9. Band gap energy of ZnO nanostructures is calculated from tauc plot using UV–VIS spectroscopy shown in Fig. 9b where  $\alpha$  is the absorption coefficient. Band gap energy is decreased with increase in pH value due to increase in the particle size (Devaraj et al. 2013). Band gap energy for pH values 3, 6 and 10.5 is 4.02, 3.77 and 3.72 (in eV), respectively. Domain size for pH values 3, 6 and 10.5 is 21, 27 and 41 (in nm), respectively. It is evident from dataset that the optical band gap tends to blue shift with decreasing domain size as pH of the solution changed from 3 to 10.5 (Tan et al. 2005).

**Raman spectroscopy**

Raman spectroscopy of ZnO nanostructures is performed for samples grown at pH value 3, 6 and 10.5. The presence of  $E_2$  (HIGH) peak for 3 different pH value ensures the good crystallinity of the sample, as shown in Fig. 10. Existence of  $E_1$  (LO) peak gives confirmation about oxygen vacancy present in our samples (Zhang et al. 2009). The Presence of  $A_1$  (LO) for pH value 10.5 confirms that the  $c$  axis of wurtzite ZnO is parallel to the sample surface (Li et al. 2013).  $2E_2$  (M) peak is related to the multi-phonon process and is assigned to the second-order Raman spectrum.  $2LO$  peak is arising due to overtone and it also

**Fig. 9** **a** The absorption spectra and **b** Tauc plot of ZnO nanostructure for pH value 3 (green line), 6 (red line), 10.5 (blue line)



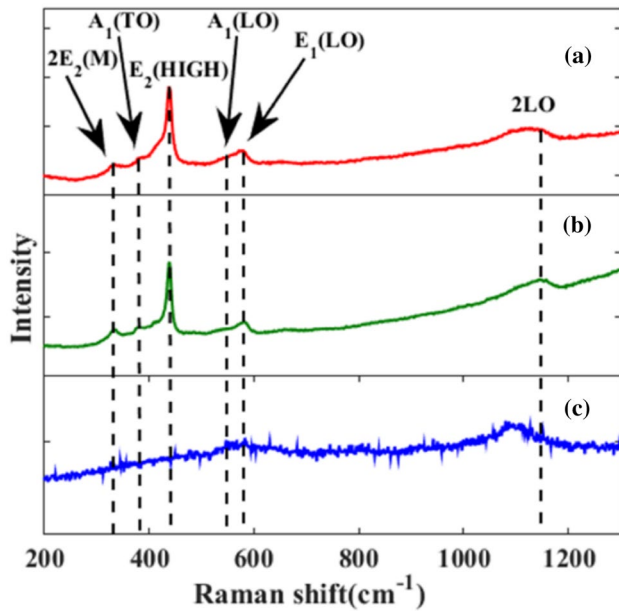


**Fig. 10** Room temperature Raman spectrum for pH value: **a** 3, **b** 6 and **c** 10.5, respectively

represents the multi-phonon scattering. Different Raman modes obtained for the samples are described in Table 2.

### Contact angle measurement

The ZnO samples grown at different pH condition show remarkable hydrophobic property. The samples grown at pH 6 show super hydrophobic surface property with static contact angle well above  $170^\circ$ . The plot of static contact angle of water as probe liquid with ZnO samples grown at different pH condition is presented in Fig. 11.

### Calculation of surface free energy

The shape of a liquid droplet is governed by the surface tensions along three interfaces namely liquid–gas ( $\gamma_l^g$ ), solid–gas ( $\gamma_s^g$ ) and solid–liquid ( $\gamma_s^l$ ) interfaces near the three-phase contact line and related to the static contact angle by the following relation:

$$\gamma_s^g = \gamma_s^l + \gamma_l^g \cos \theta_{\text{Young}}, \quad (6)$$

**Table 2** Peak values of Raman spectra for different pH values

pH value	$2E_2(\text{M})$ ( $\text{cm}^{-1}$ )	$A_1(\text{TO})$ ( $\text{cm}^{-1}$ )	$E_2(\text{HIGH})$ ( $\text{cm}^{-1}$ )	$A_1(\text{LO})$ ( $\text{cm}^{-1}$ )	$E_1(\text{LO})$ ( $\text{cm}^{-1}$ )	$2\text{LO}$ ( $\text{cm}^{-1}$ )
3	330	–	437	–	579	1130
6	334	380	437	–	580	1149
10.5	–	–	437	570	–	1194

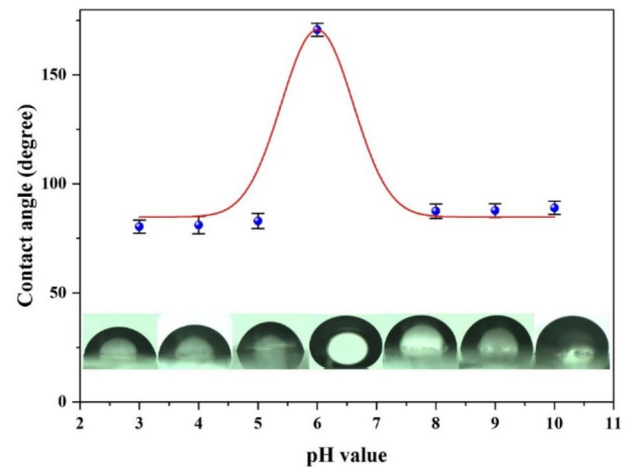


**Fig. 11** Variation of static contact angle for water as probe liquid with ZnO samples grown at different pH condition (3–10). The error bar is calculated for a set of five measurements

where  $\theta_{\text{Young}}$  is the static contact angle or contact angle of an ideal surface. The adhesive work ( $W_a$ ) and other parameters  $\gamma_l^g$ ,  $\gamma_s^g$  and  $\gamma_s^l$  are related by the following equation:

$$W_a = \gamma_l^g + \gamma_s^g - \gamma_s^l. \quad (7)$$

In this paper, the well-accepted Wendt theory is used to calculate surface free energy from the contact angle measurement (Torchinsky and Rosenman 2009). Three probe liquids (water, ethylene glycol and glycerol) with known polar and dispersive components are used for calculating surface free energy of ZnO.

$$\gamma_s^p + \gamma_s^d = \gamma_s, \quad (8)$$

$$\gamma_l^p + \gamma_l^d = \gamma_l. \quad (9)$$

The interaction between the liquid and solid adhesive work is expressed as:

$$W_a = 2 \left( \sqrt{\gamma_s^d \gamma_l^d} + \sqrt{\gamma_s^p \gamma_l^p} \right). \quad (10)$$

Combining Eqs. 6, 7 and 10 results in

$$\frac{\gamma_l(1 + \cos \theta)}{2\sqrt{\gamma_l^d}} = \frac{\sqrt{\gamma_s^p} \sqrt{\gamma_l^p}}{\sqrt{\gamma_l^d}} + \gamma_s^d. \quad (11)$$



Equation 6 can be written as  $y = mx + c$  where  $m = \sqrt{\gamma_s^p}$  and  $c = \sqrt{\gamma_s^d}$ . From slope and intercept, polar and dispersive components can be calculated. The total surface energy can be calculated from Eq. 8.

The surface energy calculated by Wendt theory using contact angle data for three different probe liquids is plotted in Fig. 12 and average values are displayed in Table 3. Three probe liquids (water, ethylene glycol and glycerol) with known polar and dispersive components are used for calculating surface free energy of ZnO.

Table 3 lists the calculated total surface energy and its polar and dispersive components for the Wendt model. As displayed in Table 3, the surface free energy of ZnO nanomaterials grown at different pH condition shows higher value in the acidic (pH 2) and alkaline region (pH 11). The surface energy of fresh ZnO nanomaterials grown at pH 2 is  $24.46 \pm$

$1.47 \text{ mN m}^{-1}$ . The surface energy of the ZnO nanomaterials decreased to  $17.96 \pm 1.06 \text{ mN/m}$  for pH 6 and then increased to  $35.51 \pm 1.65 \text{ mN m}^{-1}$  for pH11. According to the results collected from the Wendt model, the polar component of surface energy ( $\gamma_s^p$ ) is maximum for ZnO samples grown at pH 6 and increases by 73.60% and 81.67% for samples grown at pH 2 and at pH 11, whereas the dispersive component ( $\gamma_s^d$ ) decreases by 98.18% and 94.89%. The surface energy result indicates that the ZnO nanomaterials grown in the acidic (pH 2) and alkaline (pH11) condition are extremely polar and at pH 6 are extremely nonpolar in nature.

According to the results from Wendt model, the existence of a significant polar component of the total surface energy of ZnO nanomaterials grown at strong alkaline and acidic condition indicating hydrophilic ZnO surface which is consistent with the polar ZnO structure. On the contrary, ZnO nanostructures grown at pH 6 show 73.60% reduction in polar component of the surface energy leading to super hydrophobic surface, as reflected in the water static contact angle ( $170.70^\circ \pm 2.94^\circ$ ). We believe that surface roughness and microstructures are the key factors to enhance hydrophobicity in the ZnO samples.

Hydrophilic and hydrophobic nature of the ZnO nanostructures can be explained using Wenzel and Cassie-Baxter model. Figure 13 shows schematic presentation of water droplet on ZnO surface. The Wenzel region is usually recognized as homogeneous wetting, since the liquid completely penetrates into the grooves. In some circumstances, especially with the increase in the surface roughness, air pockets may be trapped in between the liquid yielding a composite interface. This heterogeneous wetting is usually described by the Cassie–Baxter (CB) model, from which the apparent contact angle ( $\theta_{CB}$ ) is given by the equation (Cassie and Baxter 1944):

$$\cos\theta_{CB} = k_1\cos\theta_A - k_2, \tag{12}$$

where  $\theta_{CB}$  is the Cassie–Baxter apparent contact angle,  $k_1$  is the solid–liquid interface to the total base area and  $k_2$  is the liquid–gas interface to the total base area. In the absence

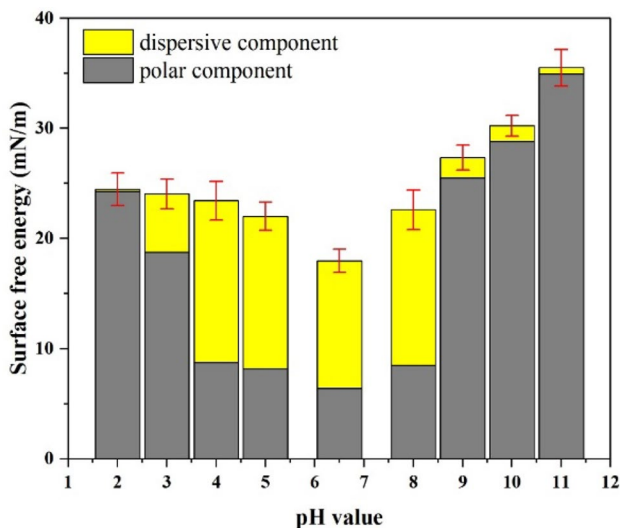
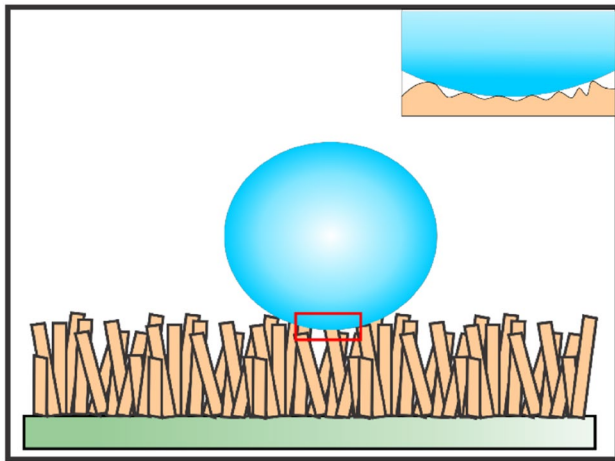


Fig. 12 Surface free energy of ZnO samples grown at different pH value. The error bar is calculated for a set of five measurements

Table 3 ZnO surface free energy along with its polar ( $\gamma^p$ ) and dispersive components ( $\gamma^d$ )

pH value of ZnO samples	Contact angle of water in degree	Polar component ( $\gamma_s^p$ ) (mN m <sup>-1</sup> )	Dispersive component ( $\gamma_s^d$ ) (mN m <sup>-1</sup> )	Surface free energy ( $\gamma_s$ ) (mN m <sup>-1</sup> )	Fraction relation of the polar to the dispersive component ( $\gamma_s^p/\gamma_s^d$ )
2	$80.12 \pm 1.29$	24.25	0.21	$24.46 \pm 1.47$	115.47
3	$80.37 \pm 2.99$	18.74	5.29	$24.03 \pm 1.35$	3.54
4	$81.12 \pm 3.92$	8.76	14.66	$23.42 \pm 1.76$	0.59
5	$83.01 \pm 3.48$	8.18	13.83	$22.01 \pm 1.28$	0.58
6	$170.70 \pm 2.94$	6.4	11.56	$17.96 \pm 1.06$	0.55
8	$87.46 \pm 3.30$	8.46	14.13	$22.59 \pm 1.79$	0.60
9	$87.80 \pm 3.12$	25.5	1.85	$27.35 \pm 1.12$	13.78
10	$89.02 \pm 3.13$	28.82	1.41	$30.23 \pm 0.95$	20.43
11	$88.98 \pm 1.22$	34.92	0.59	$35.51 \pm 1.65$	59.19



**Fig. 13** Schematic diagram of water droplet on ZnO nanorods

of air pocket,  $k_2$  becomes zero and Cassie–Baxter equation reduces to Wenzel equation. In the ZnO samples deposited at pH 6, due to dense packing of the nanorods voids are not accessible to the water droplet leading to large contact angle. Here, superhydrophobic nature of ZnO nanostructures is examined by varying the surface morphology with pH value. Due to lower value of surface free energy, ZnO nanorods are the most stable structure with super hydrophobic property which is relevant to FESEM and XRD data.

### UV photosensing characterization

The  $I$ – $V$  characteristics of the FTO/ZnO/Ag devices are obtained with bias from  $-1$  to  $+1$  V at room temperature for pH 6. Figure 14 shows the  $I$ – $V$  response for both dark and illuminated conditions of the UV sensor (pH 6). As shown in the figure, there is a visible change in  $I$ – $V$  response of the sample in dark and under UV illuminated condition. Due to larger value of surface to volume ratio for nanorods among all samples, ZnO sample grown at pH 6 shows maximum change in photocurrent under illuminated condition. The linear  $I$ – $V$  response of the devices in both dark and under UV-illuminated conditions suggests electronic contacts to be Ohmic in nature between ZnO nanostructure and silver electrodes (Dai et al. 2014; Ghosh et al. 2016). Responsivity ( $I_{ph}/P_{in}$ ) of all samples decreases as intensity increases from  $155.5$  to  $644.2 \mu\text{W cm}^{-2}$  (Fig. 15). Among all samples maximum responsivity ( $0.245 \text{ A WW}^{-1}$ ) is obtained at  $155.5 \mu\text{W/cm}^2$  for pH 6 (nanorods) and minimum responsivity ( $0.0032 \text{ A W}^{-1}$ ) is obtained at  $644.2 \mu\text{W/cm}^2$  for pH 11 (modified nanorod). Photocurrent of the fabricated UV detectors exhibits strong dependence on the incident intensity of the UV source of wavelength 365 nm. The relation between photocurrent ( $I_{ph}$ ) and the incident intensity ( $P$ ) is given as  $I_{ph} \propto P^\gamma$ . Here,  $\gamma$  determines the response

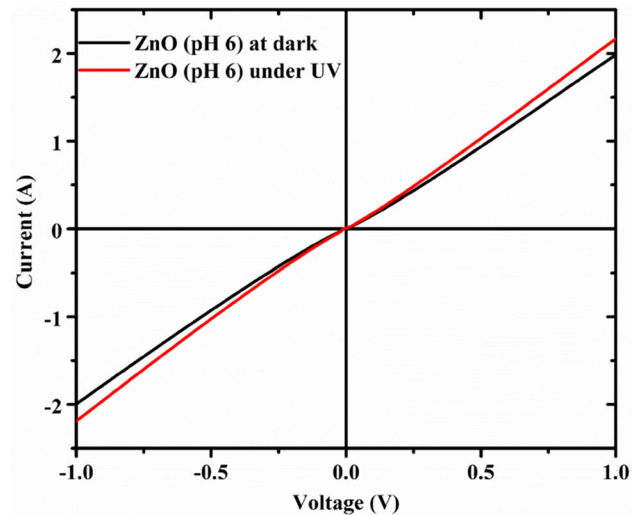


**Fig. 14**  $I$ – $V$  characteristics of ZnO nanorod (pH 6) under dark and illuminated conditions

of photocurrent to incident intensity. As incident intensity increases, more charge carriers are generated which results in more generation of photocurrent.

Here, the non-unity and a small value of  $\gamma$  suggest a complex process of electron–hole pair generation, recombination and trapping which imply the existence of defect states in the ZnO nanostructures. Figure 16a represents the photocurrent plot with incident intensity value. For pH 3, 6 and 11,  $\gamma$  values are 0.20, 0.18 and 0.61, respectively. Other calculated parameters for all three samples at  $644.2 \mu\text{W cm}^{-2}$  are shown in Table 4. Figure 16b represents the repeatability curve at intensity  $644.2 \mu\text{W cm}^{-2}$  for the sample grown at

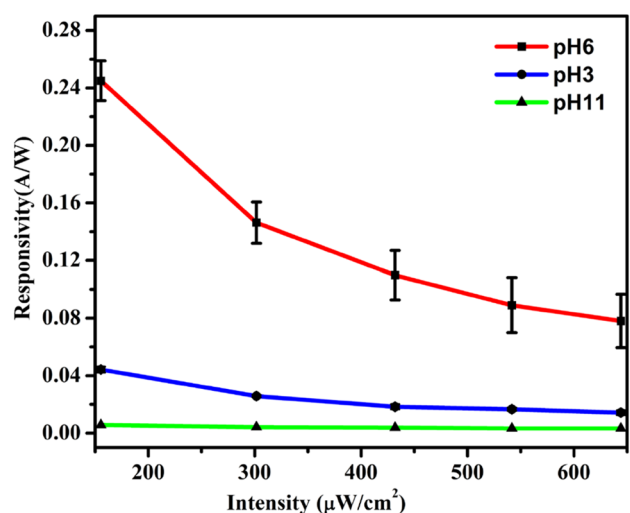


**Fig. 15** Plot of responsivity vs. intensity for all three ZnO samples. The error bars (for a set of five measurements) for pH 3 and pH 11 are smaller than the symbol size

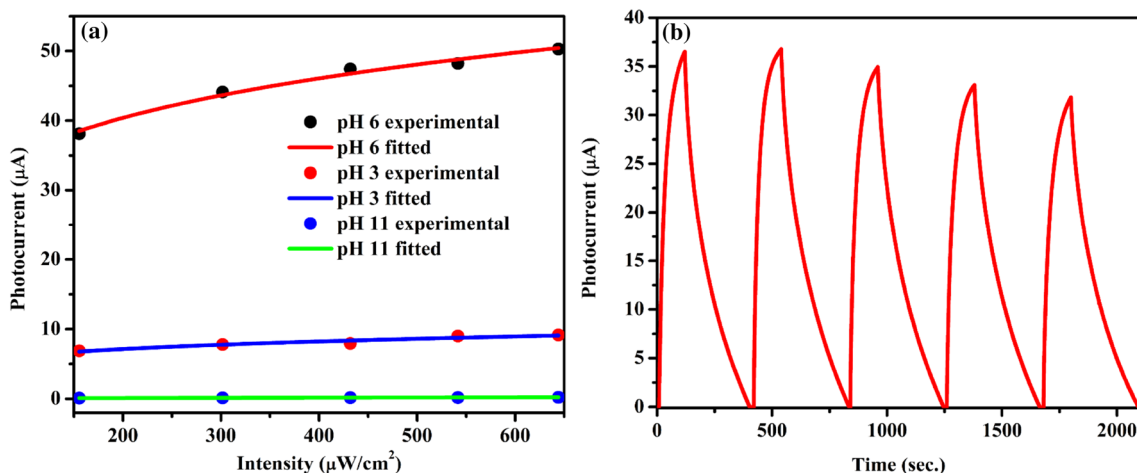


**Fig. 16** **a** Fitted and experimental plot of photocurrent vs. intensity for samples grown at pH 3, 6 and 11 and **b** repeatability curve for pH 6 at intensity 644.2 μW cm<sup>-2</sup>

**Table 4** Photocurrent, growth time and decay time for all samples at intensity 644.2 μW cm<sup>-2</sup>

pH of the samples	Photocurrent (μA)	Growth time (s)	Decay time (s)
3	9.1607	68.24 ± 1.20	238.21 ± 1.05
6	50.301	50.48 ± 1.28	248.00 ± 0.97
11	2.2299	63.79 ± 1.60	243.19 ± 1.69

pH 6. The UV source is periodically turned ‘on’ (2 min) and ‘off’ (5 min) at an interval of 7 min and repeatability data is recorded. As intensity increases, photocurrent increases. Figure 17 shows a single cycle time-resolved photocurrent measurement curve for three pH conditions at 644.2 μW cm<sup>-2</sup>. Photocurrent is maximum (50.30 μA) at 644.2 μW cm<sup>-2</sup> for pH 6 and decreases at both sides (acidic and alkali). As soon as the UV source is turned on, the increase in photocurrent is very fast followed by saturation at last. Time-resolved single cycle curve at 644.2 μW cm<sup>-2</sup> for pH 6 is shown in Fig. 18 for calculating time constants (growth and decay). The time-resolved UV photocurrent measurement of the fabricated device shows a di-exponential growth (Fig. 18). The time-dependent growth behavior of the photocurrent curve is fitted with the following bi-exponential equation.

$$I_{ph} = I_0 + A_{rf}(1 - e^{-t/\tau_{rf}}) + A_{rs}(1 - e^{-t/\tau_{rs}}), \quad (13)$$

where  $I_0$  is the dark current and  $A_{rf}$ ,  $A_{rs}$  are the positive constants and  $\tau_{rf}$  and  $\tau_{rs}$  are the fast and slow growth time constants. At intensity 644.2 μW cm<sup>-2</sup>, the time constants are 6.89±0.16 s and 35.65±0.08 s, respectively. As shown in Fig. 18, after the UV light is turned off, the decay process

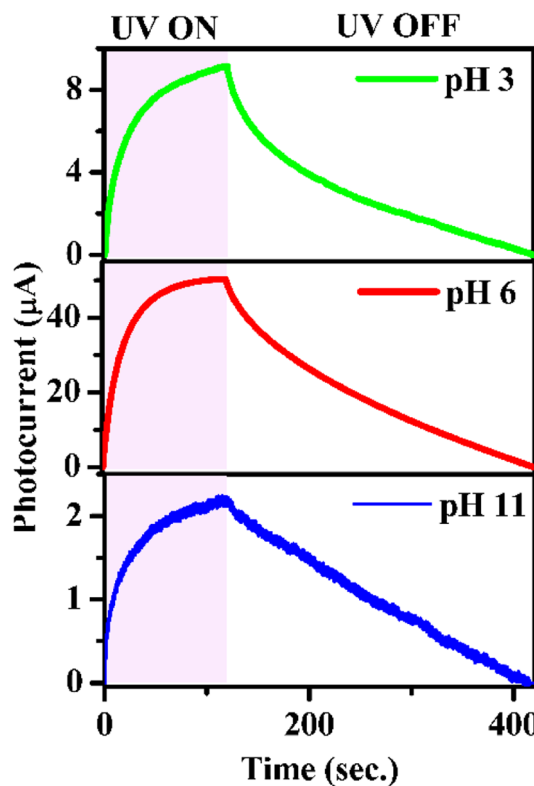


**Fig. 17** Time-resolved single cycle photoresponse curve for pH 3, 6 and 11

is fast initially and then becomes slower. The decay time behavior follows a bi-exponential decay function

$$I_{ph} = I_0 + A_{df}e^{-t/\tau_{df}} + A_{ds}e^{-t/\tau_{ds}}, \quad (14)$$

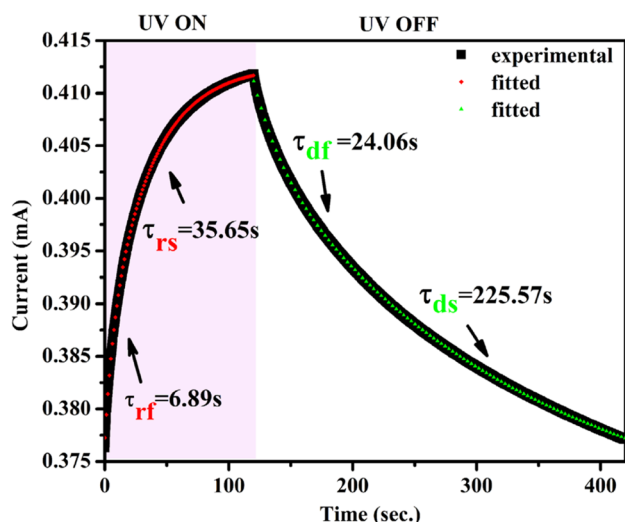


**Fig. 18** Experimental and fitted plot for photoresponse curve of pH 6 at intensity  $644.2 \mu\text{W cm}^{-2}$

where  $I_0$  is the dark current and  $A_{df}$ ,  $A_{ds}$  are positive constants and  $\tau_{df}$  and  $\tau_{ds}$  are the fast and slow decay time constants. At intensity  $644.2 \mu\text{W cm}^{-2}$ , the time constants are  $24.06 \pm 0.06 \text{ s}$  and  $225.57 \pm 0.05 \text{ s}$ . The rapid photocurrent rise can be explained by the initial excitation of electrons to higher energy states. The UV response and recovery process of ZnO nanostructure are generally guided by the water molecules and ionized oxygen adsorption and desorption at the surface defect sites. Oxygen plays a crucial role in the observed photoresponse. At room temperature, oxygen molecules are adsorbed on the nanostructure surface by capturing free electrons ( $\text{O}_2(\text{g}) + \text{e}^- \rightarrow \text{O}_2^-(\text{ad})$ ), resulting in high resistance. The density of electron–hole pairs increases significantly when illuminated under 365 nm UV light. The holes move to the surface and discharge the adsorbed oxygen ions ( $\text{O}_2^-(\text{ad}) + \text{h}^+ \rightarrow \text{O}_2(\text{g})$ ). Now, the increased value of free charge carrier concentration and the decreased width of depletion layer near the surface lead to a significant enhancement of the current. The first part of the bi-exponential photocurrent growth can be explained by the process of the photon-generated holes in ZnO nanostructures, which react with ionized oxygen on the surface and result in faster time constant  $\tau_{rf} = 6.89 \pm 0.16 \text{ s}$ . But the photocurrent cannot increase unlimitedly and it is balanced by the re-adsorption of oxygen molecules on the ZnO surface, leading to the saturation photocurrent value with a slow time constant  $\tau_{rs} = 35.65 \pm 0.08 \text{ s}$ , as indicated in the second part of the bi-exponential growth.

As the UV illumination is turned off, re-adsorption of oxygen molecules build up on the ZnO surface leading to fast decay with time constant ( $\tau_{df}$ ) of  $24.06 \pm 0.06 \text{ s}$ . The simultaneous process of capture and subsequent emission of photogenerated holes and carrier recombination (Kim

et al. 2017) are influenced by defect states present in ZnO leading to slow decay process with time constant ( $\tau_{ds}$ ) of  $225.57 \pm 0.05 \text{ sec}$ . Here, uv photoresponse of ZnO nanostructures is performed with variation of surface morphology by tuning the pH value of growth solution.

## Conclusion

In summary, ZnO nanorods with hexagonal structure and different shapes of nanoflowers are synthesized by ‘one-pot synthesis method’. Sample grown at pH 6 (nanorod) shows superhydrophobic surface with static contact angle more than  $170^\circ$  and maximum responsivity as UV photosensor. We have successfully tuned ZnO morphology from bur-flower to rod and finally rod to modified flower by varying pH of the growth solution. The results demonstrate that the overall concentration of precursors and pH values have strong influence on the morphology, ordering and properties of ZnO nanostructure. The wettability of the ZnO-coated surface is tuned by varying pH condition of the growth solution. The ratio of the polar and dispersive component of the total surface energy reaches its minimum value for pH 6. This leads us to conclude that absolute control of the surface chemical composition and microstructure is essential to attain super hydrophobicity. Under 365 nm UV illumination on–off cycle, ZnO photodetector devices show bi-exponential growth and decay characteristics. The bi-exponential growth and decay characteristics are explained with oxygen adsorption and desorption process on the surface of ZnO nanomaterials. Among all morphologies (devices), ZnO nanorod-based photodetectors show superior growth and decay time.

**Acknowledgements** The authors would like to thank UGC, India for financial support and Ms. Ria Ghosh acknowledges DST-INSPIRE, India for research fellowship.

## References

- Agnihotri S, Bajaj G, Mukherjee S, Mukherjee S (2015) Arginine assisted immobilization of silver nanoparticles on ZnO nanorods: an enhanced and reusable antibacterial substrate without human cell cytotoxicity. *Nanoscale* 7:7415–7429
- Cassie ABD, Baxter S (1944) Wettability of porous surfaces. *Trans Faraday Soc* 40:546–551
- Chang WC, Cheng YY, Yu WC, Yao YC, Lee CH, Ko HH (2012) Enhancing performance of ZnO dye-sensitized solar cells by incorporation of multiwalled carbon nanotubes. *Nanoscale Res Lett* 7:166
- Chen J, Min F, Liu L (2019) The interactions between fine particles of coal and kaolinite in aqueous, insights from experiments and molecular simulations. *Appl Surf Sci* 467–468:12–21
- Chithra MJ, Sathya M, Pushpanathan K (2015) Effect of pH on crystal size and photoluminescence property of ZnO nanoparticles prepared by chemical precipitation method 28:394–404

- Choi MY, Choi D, Jin MJ, Kim I, Kim SH, Choi JY, Lee SY, Kim JM, Kim SW (2009) Mechanically powered transparent flexible charge-generating nanodevices with piezoelectric ZnO nanorods. *Adv Mater* 21(21):2185–2189
- Dai W, Pan X, Chen C, Chen S, Chen W, Zhang H, Ye Z (2014) Enhanced UV detection performance using a Cu-doped ZnO nanorod array film. *RSC Adv* 4:31969–31972
- Demianets LN, Kostomarov DV, Kuz'mina IP, Pushko SV (2002) Mechanism of growth of ZnO single crystals from hydrothermal alkali solutions. *Crystallogr Rep* 47:S86–S98
- Devaraj R, Karthikeyan K, Jeyasubramanian K (2013) Synthesis and properties of ZnO nanorods by modified pechini process. *Appl Nanosci* 3:37–40
- Dimapilis EAS, Hsu CS, Mendoza RMO, Lu MC (2018) Zinc oxide nanoparticles for water disinfection. *Sustain Env Res* 28:47–56
- Djurišić AB, Chen X, Leung YH, Man CN (2012) ZnO nanostructures: growth, properties and applications. *J Mater Chem* 22:6526–6535
- Doan VY, Vuong PH, Lan H, Tam PD (2016) Synthesis of ZnO nanorod for immunosensor application. *Vietnam J Chem* 54(6):765–770
- Ghosh SP, Das KC, Tripathy N, Bose G, Kim DH, Lee TI, Myoung JM, Kar JP (2016) Ultraviolet photodetection characteristics of Zinc oxide thin films and nanostructures. *IOP Conf Ser Mater Sci Eng* 115:012035
- Khokhra R, Bharti B, Lee HN, Kumar R (2017) Visible and UV photodetection in ZnO nanostructured thin films via simple tuning of solution method. *Sci Rep* 7:15032
- Khranovskyy V, Yakimova R (2012) Morphology engineering of ZnO nanostructures. *Phys B* 407:1533–1537
- Kim D, Kim W, Jeon S, Yong K (2017) Highly efficient UV-sensing properties of Sb-doped ZnO nanorod arrays synthesized by a facile, single-step hydrothermal reaction. *RSC Adv* 7:40539–40548
- Kumar M, Jeong H, Lee D (2019) UV photodetector with ZnO nanoflowers as an active layer and a network of Ag nanowires as transparent electrodes. *Superlattices Microstruct* 126:132–138
- Kundu S, Majumder R, Ghosh R, Pal Chowdhury M (2019) Superior positive relative humidity sensing properties of porous nanostructured Al:ZnO thin films deposited by jet-atomizer spray pyrolysis technique. *J Mater Sci Mater Electron* 2019:1–8
- Lee M, Kwak G, Yong K (2011) Wettability control of ZnO nanoparticles for universal applications. *ACS Appl Mater Interfaces* 3:3350–3356
- Li WJ, Shi EW, Zhong WZ, Yin ZW (1999) Growth mechanism and growth habit of oxide crystals. *J Cryst Growth* 203:186–196
- Li S, Hu J, Li J, Tian J, Han Z, Zhou X, Chen Y (2011) Anisotropic wet etched silicon substrates for reoriented and selective growth of ZnO nanowires and enhanced hydrophobicity. *Langmuir* 27:6549–6553
- Li CP, Zhang J, Yu HM, Zhang LJ (2013) Raman and photoluminescence properties of ZnO Nanorods with wurtzite structure. *Key Eng Mater* 538:50–53
- Medina J, Bolaños H, Mosquera-Sanchez LP, Rodriguez-Paez JE (2018) Controlled synthesis of ZnO nanoparticles and evaluation of their toxicity in *Mus musculus* mice. *Int Nano Lett* 8:165–179
- Motevalizadeh L, Heidary Z, Abrishami ME (2014) Facile template-free hydrothermal synthesis and microstrain measurement of ZnO nanorods. *Bull Mater Sci* 37:397–405
- Mudunkotuwa IA, Rupasinghe T, Wu CM, Grassian VH (2012) Dissolution of ZnO nanoparticles at circumneutral pH: a study of size effects in the presence and absence of citric acid. *Langmuir* 28:396403
- Orlov A, Ulianova V, Zazerin A, Bogdan O, Pashkevich G, Yakymenko Y (2016) Active elements on a basis of ZnO nanorods for energy harvesting devices. *Radioelectron Commun Syst* 59:60–65
- Park JH, Park JH, Biswas P, Kwon DKH, Sun W, Baik HK, Myoung JM (2016) Adopting novel strategies in achieving high-performance single-layer network structured ZnO nanorods thin film transistors. *ACS Appl Mater Interfaces* 8:11564–11574
- Peng X, Wang W, Zeng Y, Pan X, Ye Z, Zeng Y (2018) Enhanced photoresponse of a high-performance self-powered UV photodetector based on ZnO nanorods and a novel electrolyte by the piezo-phototronic effect. *R Soc Chem* 8:33174–33179
- Prakash GV, Pradeesh K, Kumar A, Kumar R, Rao SV, Markham M, Baumberg J (2008) Morphological manipulation of the nonlinear optical response of ZnO thin films grown by thermal evaporation. *Mater Lett* 62:1183–1186
- Purwaningsih SY, Pratapa S, Triwikantoro, Darminto (2016) Nano-sized ZnO powders prepared by coprecipitation method with various pH. *AIP Conf Proc* 1725:020063
- Ramimoghadam D, Hussein M, Taufiq-Yap YH (2013) Synthesis and characterization of ZnO nanostructures using palm olein as biotemplate. *Chem Cent J* 7:71
- Rodwihok C, Choopun S, Ruankham P, Gardchareon A, Phadungdhitidhada S, Wongratanaphisan D (2017) UV sensing properties of ZnO nanowires/nanorods. *Appl Surf Sci*. <https://doi.org/10.1016/j.apsusc.2017.11.056>
- Sarahnaz S, Gujela OP, Afzulpurkar NV (2013) Fabrication of light emitting diode with ZnO nanorods on polymer coated silicon substrate. *Int Conf Manipul Manuf Meas Nanoscale* 2013:295–298
- Sarangi SN (2016) Controllable growth of ZnO nanorods via electrode position technique: towards UV photodetection. *J Phys D Appl Phys* 49:355103
- Sarkar S, Basak D (2015) Understanding of ultraviolet photoresponse properties of ZnO nanorods: effect of nanorod's size and ambient. *Sci Lett J* 5:4
- Sasmal AK, Mondal C, Sinha AK, Gauri SS, Pal J, Aditya T, Ganguly M, Dey S, Pal T (2014) Fabrication of superhydrophobic copper surface on various substrates for roll-off, self-cleaning, and water/oil separation. *ACS Appl Mater Interfaces* 6:22034–22043
- Schuster JM, Schvezov CE, Rosenberger MR (2015) Analysis of the results of surface free energy measurement of Ti<sub>6</sub>Al<sub>4</sub>V by different methods. *Procedia Mater Sci* 8:732–741
- Selvarajan E, Mohanasrinivasan V (2013) Biosynthesis and characterization of ZnO nanoparticles using *Lactobacillus plantarum* vites 07. *Mater Lett* 112:180–182
- Shahabi S, Najafi F, Majdabadi A (2014) Effect of gamma irradiation on structural and biological properties of a PLGA-PEG-hydroxyapatite composite. *Sci World J* 2014:1–9
- Shaikh SK, Ganbavle VV, Inamdar SI, Rajpure KY (2016) Multifunctional zinc oxide thin films for high-performance UV photodetectors and nitrogen dioxide gas sensors. *RSC Adv* 6:25641–25650
- Sirelkhatim A, Mahmud S, Seeni A, Kaus NHM, Ann LC, Bakhori SKM, Hasan H, Mohamad D (2015) Review on zinc oxide nanoparticles: antibacterial activity and toxicity mechanism. *Nano-Micro Lett* 7:219–242
- Smeraldi J, Ganesh R, Hosseini T, Khatib L, Olson B, Rosso D (2017) Fate and toxicity of zinc oxide nanomaterial in municipal wastewaters. *Water Environ Res* 89:880–889
- Soci C, Zhang A, Xiang B, Dayeh SA, Aplin DPR, Park J, Bao XY, Lo YH, Wang D (2007) ZnO nanowire UV photodetectors with high internal gain. *Nano Lett* 7:1003–1009
- Sohn JI, Hong WK, Lee S, Lee S, Ku J, Park YJ, Hong J, Hwang S, Park KH, Warner JH, Cha S, Kim JM (2014) Surface energy-mediated construction of anisotropic semiconductor wires with selective crystallographic polarity. *Sci Rep* 4:5680
- Stalder AF, Melchior T, Müller M, Sage D, Blu T, Unser M (2010) Low-bond axisymmetric drop shape analysis for surface tension and contact angle measurements of sessile drops. *Colloids Surf A Physicochem Eng Aspects* 364:72–81

- Sun B, Siringhaus H (2005) Solution-processed zinc oxide field-effect transistors based on self-assembly of colloidal nanorods. *Nano Lett* 12:2408–2413
- Sun ZP, Liu L, Zhang L, Jia DZ (2006) Rapid synthesis of ZnO nanorods by one-step, room-temperature, solid-state reaction and their gas-sensing properties. *Nanotechnology* 17(9):2266
- Tak M, Gupta V, Tomar M (2015) A highly efficient urea detection using flower-like zinc oxide nanostructures. *Mater Sci Eng C* 57:38–48
- Talam SA, Karumuri SRA, Gunnam NA (2012) Synthesis, characterization, and spectroscopic properties of ZnO nanoparticles, *ISRN Nanotechnol* 2012:6
- Tan ST, Chen BJ, Sun XW, Fan WJ, Kwok HS, Zhang XH, Chua SJ (2005) Blue shift of optical band gap in ZnO thin films grown by metal-organic chemical-vapor deposition. *J Appl Phys* 98:013505
- Torchinsky I, Rosenman G (2009) Wettability modification of nanomaterials by low-energy electron flux. *Nanoscale Res Lett* 4:1209–1217
- Udom I, Ram MK, Stefanakos EK, Hepp AF, Goswami DY (2013) One dimensional-ZnO nanostructures: synthesis, properties and environmental applications. *Mater Sci Semicond Process* 16:2070–2083
- Vicente CMS, André PS, Ferreira RAS (2012) Simple measurement of surface free energy using a web cam. *Rev Brasil Ensino Fisica* 34:1–5
- Wahab R, Ansari S, Kim Y, Seo H, Kim G, Khang G, Shin HS (2007) Low temperature solution synthesis and characterization of ZnO nano-flowers. *Mater Res Bull* 42:1640–1648
- Wang Z (2004) Zinc oxide nanostructures: growth, properties and applications. *J Phys Condens Matter* 16:R829
- Wang B, Zhang Z, Chang K, Cui J, Rosenkranz A, Yu J, Lin CT, Chen G, Zang K, Luo J, Jiang N, Guo D (2018) New deformation-induced nanostructure in silicon. *Nano Lett* 18:4611–4617
- Wenzel RN (1936) Resistance of solid surfaces to wetting by water. *Ind Eng Chem* 28:988–994
- Yin YT, Wu SH, Chen CH, Chen LY (2011) Fabrication of ZnO nanorods in one pot via solvothermal method. *J Chin Chem Soc* 58:749–755
- Yin Y, Sun Y, Yu M, Liu X, Yang B, Liu D, Liu S, Cao W, Ashfold MNR (2014) Controlling the hydrothermal growth and the properties of ZnO nanorod arrays by pre-treating the seed layer. *RSC Adv* 4:44452–44456
- Zanni E, Bruni E, Chandraiaghari CR, De Bellis G, Santangelo MG, Leone M, Bregnocchi A, Mancini P, Sarto MS, Uccelletti D (2017) Evaluation of the antibacterial power and biocompatibility of zinc oxide nanorods decorated graphene nanoplatelets: new perspectives for antibiodeteriorative approaches. *J Nanobiotechnol* 15:57
- Zhai T, Xie S, Zhao Y, Xiaofeng S, Lu X, Yu M, Xu M, Xiao F, Tong Y (2012) Controllable synthesis of hierarchical ZnO nanodisks for highly photocatalytic activity. *Cryst Eng Comm* 14:1850–1855
- Zhang R, Yin PG, Wang N, Guo L (2009) Photoluminescence and Raman scattering of ZnO nanorods. *Solid State Sci* 11:865–869
- Zhang Z, Song Y, Huo F, Guo D (2012a) Nanoscale material removal mechanism of soft-brittle HgCdTe single crystals under nanogrinding by ultrafine diamond grits. *Tribol Lett* 46:95–100
- Zhang Z, Song Y, Xu C, Guo D (2012b) A novel model for undeformed nanometer chips of soft-brittle HgCdTe films induced by ultrafine diamond grits. *Scr Mater* 67:197–200
- Zhang Z, Huo F, Zhang X, Guo D (2012c) Fabrication and size prediction of crystalline nanoparticles of silicon induced by nanogrinding with ultrafine diamond grits. *Scr Mater* 67:657–660
- Zhang G, Wei L, Chen Y, Mei L, Jiao J (2013a) Field emission property of ZnO nanoneedle arrays with different morphology. *Mater Lett* 96:131–134
- Zhang Z, Huo Y, Guo D (2013b) A model for nanogrinding based on direct evidence of ground chips of silicon wafers. *Sci China Technol Sci* 56:2099–2108
- Zhang Z, Wang B, Kang R, Zhang B, Guo D (2015) Changes in surface layer of silicon wafers from diamond scratching. *CIRP Ann* 64:349–352
- Zhang Z, Wang B, Huang S, Wen B, Yang S, Zhang B, Lin CT, Jiang N, Jin Z, Guo D (2016a) A novel approach to fabricating a nanotwinned surface on a ternary nickel alloy. *Mater Design* 106:313–320
- Zhang Z, Wang B, Zhou P, Kang R, Zhang B, Guo D (2016b) A novel approach of chemical mechanical polishing for cadmium zinc telluride wafers. *Sci Rep* 6:26891
- Zhang Z, Wang B, Zhou P, Guo D, Kang R, Zhang B (2016c) A novel approach of chemical mechanical polishing using environment-friendly slurry for mercury cadmium telluride semiconductors. *Sci Rep* 6:22466
- Zhang Z, Huang S, Chen L, Wang B, Wen B, Zhang B, Guo D (2017a) Ultrahigh hardness on a face-centered cubic metal. *Appl Surf Sci* 416:891–900
- Zhang Z, Cui J, Wang B, Wang Z, Kang R, Guo D (2017b) A novel approach of mechanical chemical grinding. *J Alloy Compd* 726:514–524
- Zhang Z, Shi Z, Du Y, Yu Z, Guo L, Guo D (2018) A novel approach of chemical mechanical polishing for a titanium alloy using an environment-friendly slurry. *Appl Surf Sci* 427:409–415
- Zhang Z, Cui J, Zhang J, Liu D, Yu Z, Guo D (2019) Environment friendly chemical mechanical polishing of copper. *Appl Surf Sci* 467–468:5–11

**Publisher's Note** Springer Nature remains neutral with regard to jurisdictional claims in published maps and institutional affiliations.